CORROSION SCIENCE AND TECHNOLOGY, Vol.23, No.6(2024), pp.471~481 pISSN 1598-6462 / eISSN 2288-6524
[Research Paper] DOI: https://doi.org/10.14773/cst.2024.23.6.471

Effects of Welding Current and Speeds in Plasma Arc Welding on Microstructures and Mechanical Properties of 304 Stainless Steel and Acid Pickling Behaviors

Taek Gyu Kwon, Hye Seong Seo, Eun Chan Wang, Sung Jin Kim†, and Yi Je Cho†

Department of Materials Science and Metallurgical Engineering, Sunchon National University, 255 Jungang-ro, Suncheon-si, Jeollanam-do, 57922 Republic of Korea

(Received November 11, 2024; Revised November 22, 2024; Accepted November 23, 2024)

The effects of welding current and speed in plasma arc welding (PAW) on the microstructures and mechanical properties of 304 stainless steel and its acid pickling behavior were investigated. 304 stainless steel pipes were fabricated using PAW at nine different welding currents and speeds. The resulting weld was composed of austenite and δ-ferrite, where the dendritic structure size decreased as heat input was reduced. At a constant welding speed, increasing the current improved elongation, while the strength remained nearly unchanged. After heat treatment, an oxide layer formed, consisting of $(Mn, Cr, Fe)_3O_4$ spinel, Ni-rich metallic phase, Fe_3O_4, and Fe_2O_3. During acid pickling, the oxide layer on the weld was removed more rapidly than that on the base metal due to the formation of a Cr- and Mn-enriched layer within the inner oxide. As the number of specimens increased, the time required for effective acid pickling also increased, while the mass loss rate decreased. An equation was proposed to estimate the pickling performance of the acid solution.

Keywords: *304 Stainless steel, Plasma arc welding, Acid pickling, Microstructure, Mechanical property*

1. Introduction

Stainless steels are alloys that contain additional elements, including Cr and Ni, to improve corrosion resistance to air, water, and chemicals. Among them, 304 stainless steels (304SS) have austenitic microstructures that offer excellent corrosion and wear resistance, weldability, and formability, with typical applications in chemical and petrochemical processing, machinery, and structural components of ships, aircraft, and automobiles [1-3]. Additionally, jet propellants, gas turbines, and nuclear plants are other applications due to their high temperature and pressure toughness [4,5].

Plasma arc welding (PAW) is an effective method for joining 304SS workpieces with thicknesses ranging from 6 to 13 mm, using a non-consumable tungsten electrode to ignite and maintain an arc in the weld zone [6,7]. Studies have focused on PAW processing parameters to elucidate their effects on microstructures and mechanical properties, including activating flux, current, welding speed, plasma flow rate, working distance, and current mode [8-13]. Activating flux improved penetration depth by constricting the plasma column and reducing the anode spot [8]. An increase in plasma flow rate led to greater penetration depth and grain size, while a slight decrease could destabilize the process [7,9,11]. Working distance affected energy loss, resulting in undercutting or incomplete penetration [7,11,12]. Increased welding current improved mechanical properties, but coarser δ-ferrite formation in the fusion zone at high current reduced strength and hardness [12]. Pulse current mode demonstrated superior impact properties compared to constant current mode, owing to higher dislocation density and martensite volume fraction [13].

Post-weld heat treatment of 304SS is performed after PAW to reduce microstructural inhomogeneity, residual stress, brittleness, and the toughness loss that occur during welding [5,14]. Since the heat treatment is conducted in air, oxide layers with various compositions of Fe, Cr, Ni, and O form on the surface [15,16]. Additionally, preferential oxidation of Cr to Cr_2O_3 or a spinel results in a significant

†Corresponding author: sjkim56@scnu.ac.kr, yijecho@scnu.ac.kr
Taek Gyu Kwon: Ph.D. Student, Hye Seong Seo: Master Student, Eun Chan Wang: Bachelor Student, Sung Jin Kim: Professor, Yi Je Cho: Professor

Cr-depleted zone beneath the oxide scale, which can lead to intergranular corrosion or stress corrosion cracking in this zone [16]. To achieve fine surface quality and remove the Cr-depleted zone, acid pickling can be applied, allowing acid to penetrate through the pores and cracks in the oxide layers, attacking the FeO layer and releasing the relatively insoluble Fe_2O_3 and Fe_3O_4 layers above [15,16]. Acid solutions commonly used for pickling stainless steels include H_2SO_4 [17,18], HCl [19-22], HF [22,23], HNO_3 [16], and/or their mixtures [23-26]. Although HNO_3 and its mixtures were traditionally used, use has diminished due to NO_x emissions, which raise environmental concerns [16,23]. HCl solutions can dissolve both the oxide and base metal, but corrosion from chloride remains an issue [19-22]. HF solutions effectively dissolve oxide scales, particularly SiO_2 [22, 23]. H_2SO_4 is widely used in practice due to low cost and chemical stability and is often mixed with HF [18,23]. Many studies have investigated the effects of acid concentration, immersion time, pickling type (static or dynamic and single- or multi-step), and oxidant addition on pickling behavior and microstructures [16-26].

Although various studies have examined the effects of PAW conditions and acid pickling, notable gaps remain between lab-scale experiments and industrial applications. For instance, the general pickling process includes mechanical descaling, preliminary pickling, and final pickling [16,18]. However, mechanical descaling and preliminary pickling steps are often omitted in actual industrial processes due to limitations in facility capabilities, cost, and manpower. To bridge this gap, a detailed study considering practical processing conditions is necessary to understand the relationship between PAW processing conditions and microstructures, mechanical properties, and acid pickling behavior. This study investigated the effects of welding current and speed in PAW on the microstructures, mechanical properties, and acid pickling behavior of 304SS. Samples were welded and heat-treated based on industry-standard processing conditions to assess the effects. Similarly, the acid solution and additives used in industry were directly utilized to evaluate pickling behavior. Microstructures, chemical composition, tensile properties, and fracture surfaces after welding were analyzed, followed by a discussion of acid pickling behavior across different cycles.

2. Experimental Procedures

A plate of raw 304SS with a thickness of 5 mm was obtained from POSCO, Republic of Korea. A pipe with an outer diameter of 406.4 mm and a length of 3000 mm was fabricated by PAW using the 304SS plate, following the processing conditions listed in Table 1, with a length of 300 mm for each condition. 308L stainless steel was used as the welding filler wire. The chemical compositions of 304 and 308L stainless steels can be found elsewhere [5]. After joining the outer surface of the pipes using PAW, gas tungsten arc welding was performed on both the inner and outer surfaces once more, respectively. Post-weld heat treatment for the pipes was conducted at 1050 °C for 10.8 min in air, followed by cooling in flowing water. Acid pickling of the heat-treated pipes was performed on small specimens, cut to a 5 × 30 × 30 mm^3 dimension with the welded section at the center. The pickling solution of 200 mL was prepared by mixing 8 vol% HF, 10 vol% H_2SO_4, and 82 vol% H_2O. Rust powder (10 g), which detached from the pipes after heat treatment and consisted of Fe_2O_3 and Fe_3O_4 (Fig. 1), was dissolved in the pickling solution as an oxidant to accelerate the pickling rate. Acid pickling was conducted at 60 °C, with the solution covered during pickling to minimize evaporation. The acid pickling process was considered complete when the black oxide scale covering the specimen surface was fully removed.

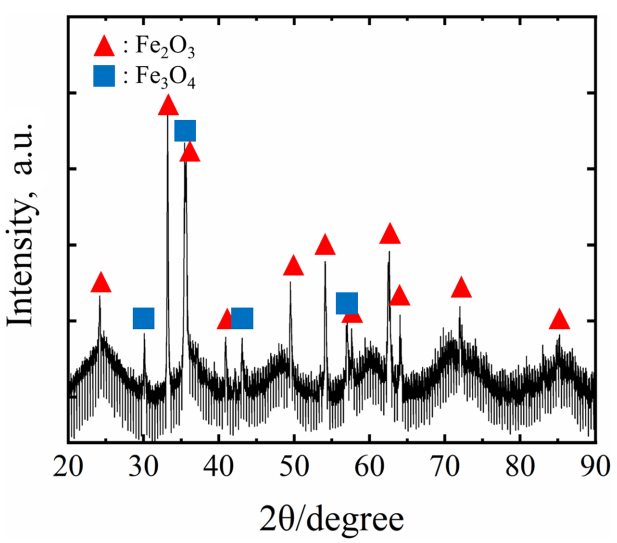

Fig. 1. An X-ray diffraction pattern of rust powder dissolved into the pickling solution

Table 1. Processing conditions of the PAW for 304SS

Condition	Current (A)	Voltage (V)	Welding speed (cm/min)	Heat input (J/mm/s)
1	250	27	50	810
2	275	27	50	891
3	300	27	50	972
4	250	27	55	736
5	275	27	55	810
6	300	27	55	883
7	250	27	60	675
8	275	27	60	742
9	300	27	60	810

For mechanical testing of the welded pipes before heat treatment, the pipes were machined into tensile specimens with the welded section in the middle, following the ASTM E-8 standard [27]. The tensile specimens were flattened using a hydraulic press to remove curvature before testing. The specimens were elongated at a strain rate of 10^{-3} s^{-1} until fracture. The tests were performed three times to ensure the repeatability and reproducibility of the results. Microstructures and phases were characterized by an optical microscope (OM), scanning electron microscope (SEM) with energy dispersive spectroscopy (EDS), and X-ray diffractometer (XRD). Porosity was evaluated through image analysis using ImageJ. The mass change of the specimens during acid pickling was measured every 10 min. After 40 min of pickling, the immersed specimens were gently brushed to remove the oxide scale.

3. Results and Discussion

3.1 Effects of welding conditions on microstructures and mechanical properties

Microstructures in the welds of specimens fabricated under various welding conditions are shown in Fig. 2. The bright dendritic phase is austenite, while the dark interdendritic phase is δ-ferrite. No equiaxed grains were observed. These microstructural features suggest that the substructure grows in the direction of the highest temperature gradient [13]. Differences in dendrite size and spacing are evident between the welding conditions. High heat input resulted in a low cooling rate, leading to coarse dendritic structures, while a steep thermal gradient developed with low heat input, forming finer microstructures [6,28]. In addition, both skeletal and lathy δ-ferrite were observed regardless of the welding condition, although the relative amounts of each shape varied. The formation of differently shaped ferrite is also attributed to the cooling rate [5,29]. Skeletal δ-ferrite forms at a low cooling rate, which provides sufficient time for austenite to consume existing ferrite. This occurs in conditions with high heat input (conditions 2, 3, and 6), where the amount of skeletal δ-ferrite is greater than that of lathy δ-ferrite. Under high cooling rates, diffusion in the ferrite-austenite transformation is limited, leading to the formation of lathy δ-ferrite (conditions 4, 7, and 8).

The elemental distribution in the weld obtained under condition 6 is shown in Fig. 3. It is clearly seen that δ-ferrite is enriched with Cr. The segregation of Cr is influenced by the cooling rate; the degree of segregation decreases as the cooling rate increases, while the partition coefficient between austenite and δ-ferrite remains lower than unity [30,31]. Simultaneously, the depletion of austenite-promoting elements such as Ni is known to occur, but this behavior was undetectable due to the small difference in Ni content (< 2 wt%) between austenite and δ-ferrite [30].

The mechanical properties of specimens welded under different conditions are presented in Fig. 4. All specimens fractured at the weld. The yield and tensile strengths obtained with a welding speed of 50 cm/min (conditions 1–3) decrease as the current increases from 250 to 300 A. However, at constant welding speeds of 55 cm/min (conditions 4–6) and 60 cm/min (conditions 7–9), both strength values remain nearly the same regardless of the

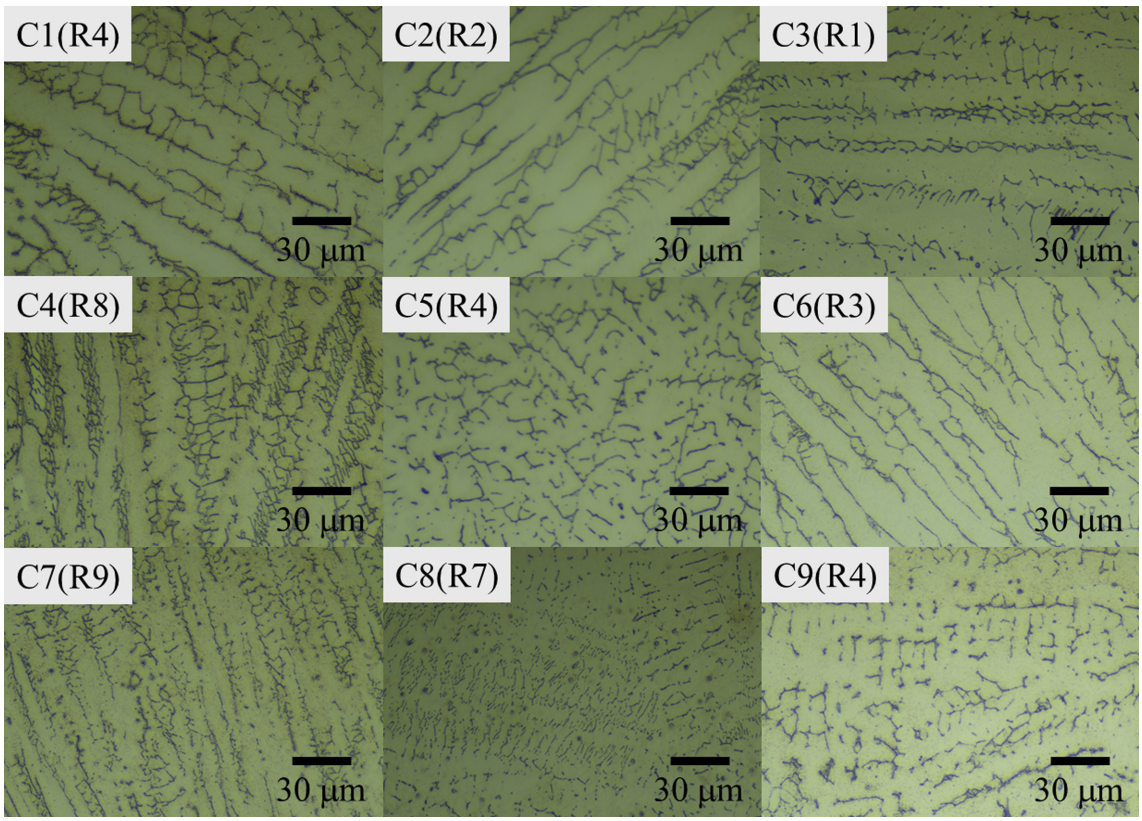

Fig. 2. OM images of the weld area in the 304SS specimens fabricated by the various welding conditions. The 'C' number and ('R' number) in each image indicate the welding condition and the ranking of heat input, respectively

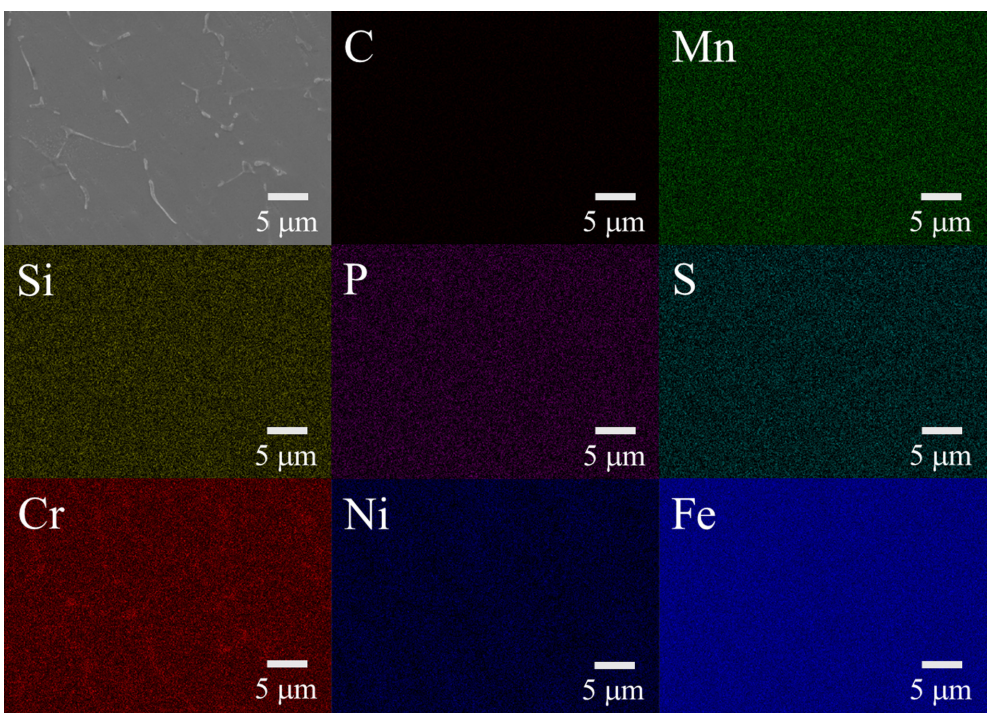

Fig. 3. Elemental mapping of the microstructure in the weld obtained with the welding condition 6

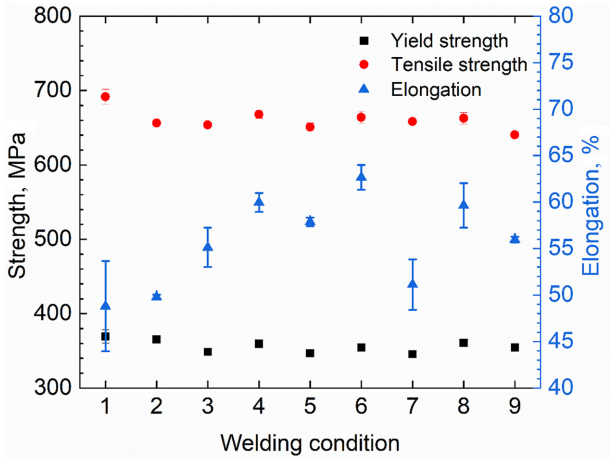

Fig. 4. Strength and elongation of the 304 stainless steel specimens welded by various welding conditions

current. The overall ranges of yield and tensile strength were 355–369 MPa and 641–692 MPa, respectively. Conversely, increasing the current at a constant welding speed tends to raise the elongation. The highest elongation, with moderate yield and tensile strengths, was achieved under welding condition 6, while welding condition 1 showed the lowest ductility.

The fracture surfaces of the tensile specimens welded under conditions 1, 6, and 7 are shown in Fig. 5. Uneven surfaces with different heights were observed in the specimens from conditions 1 and 7 (Fig. 5a and c). These surfaces were composed of flat cleavage areas with dimples in between, indicating a combination of ductile and brittle fractures. In contrast, uniform surfaces with similar heights were found in the specimen from condition 6 (Fig. 5b). Dimples covered these surfaces, indicating that ductile fracture was dominant. The fracture surfaces in Fig. 5 illustrate the differences in elongation among the specimens. The porosity in the weld of all specimens was less than 0.05%, as determined by image analysis. Only in the weld from condition 9 was the porosity 0.11%, which likely contributed to the lowest tensile strength among the specimens.

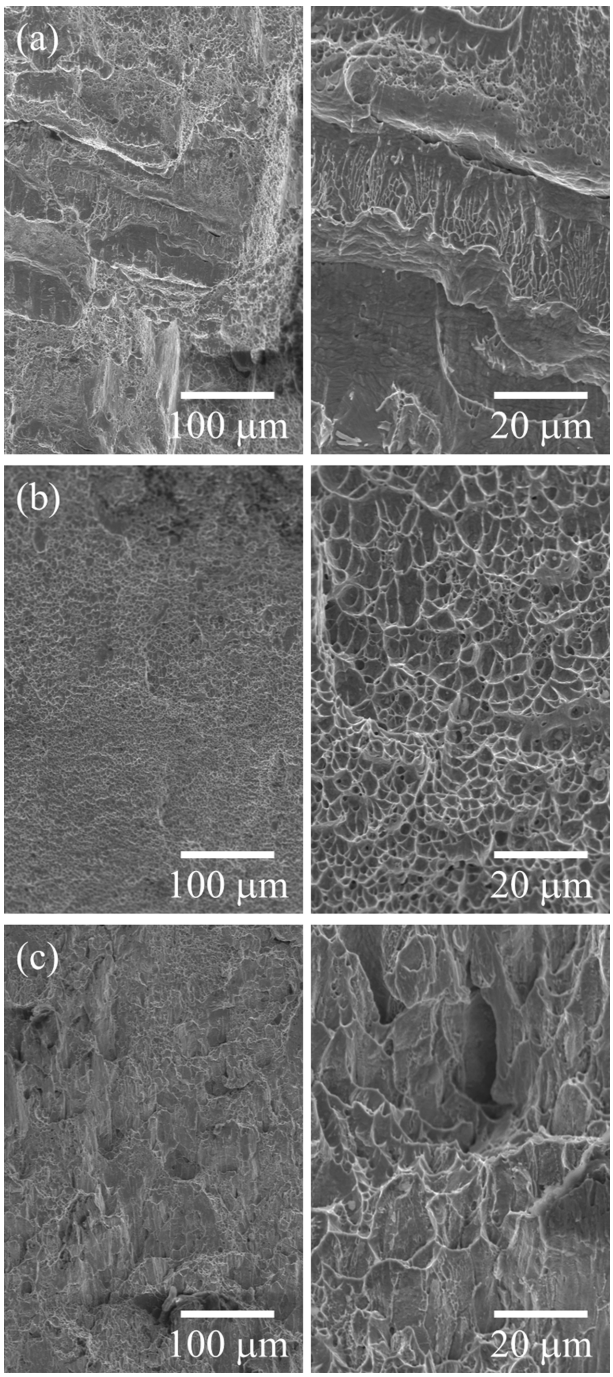

Fig. 5. Fracture surfaces of the 304 stainless steel specimens, welded by the conditions (a) 1, (b) 6, and (c) 7, at two different magnifications

3.2 Acid Pickling Behaviors

The subsequent heat treatment and acid pickling were conducted on specimens fabricated under welding condition 6, which achieved the highest ductility and moderate strength. The cross-sections and corresponding elemental distributions in the base metal and weld of the heat-treated specimens are shown in Fig. 6. The oxide thickness in the base metal and weld was 10.9 ± 3.6 and 11.7 ± 2.7 mm, respectively (Fig. 6a and b). Cracks were observed in the oxide layer, forming in both vertical and horizontal directions. Differences in thermal expansion behavior of the base metal and oxide and the applied load

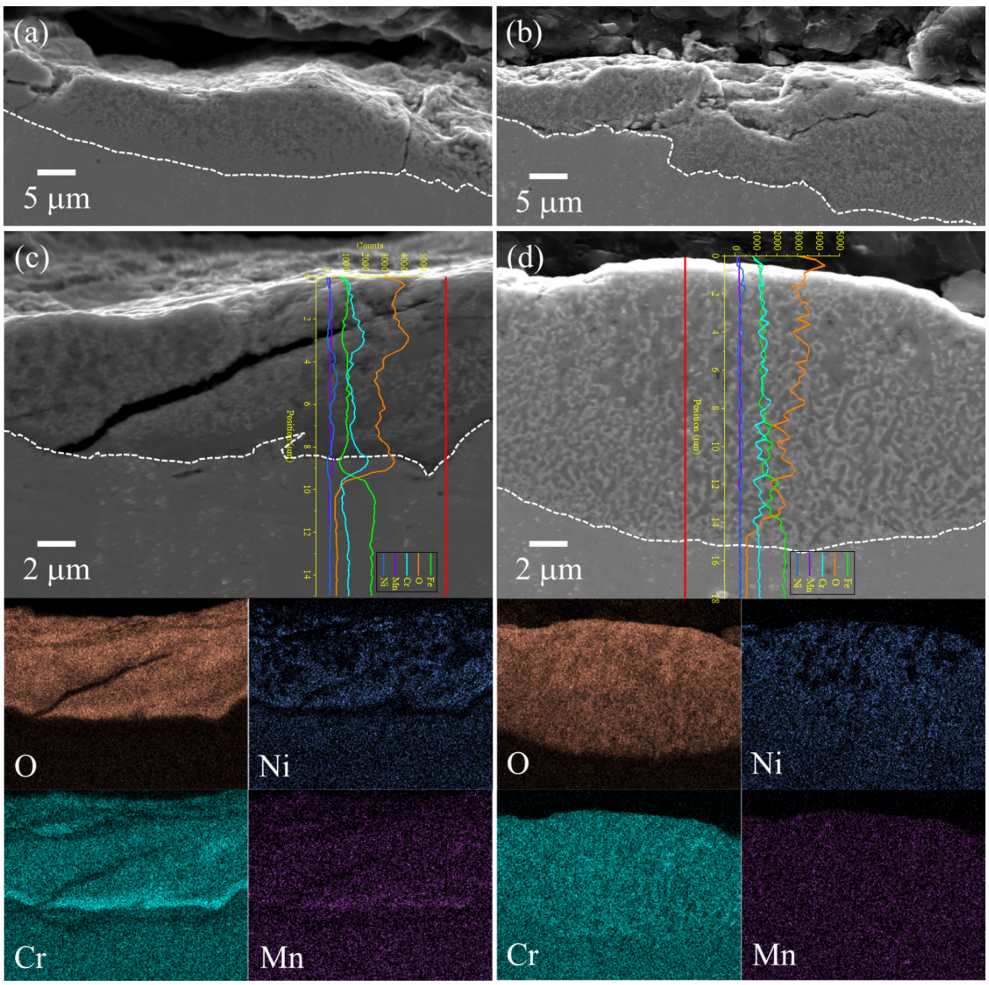

Fig. 6. SEM cross-sections of (a) base metal and (b) weld and elemental distributions along the thickness direction in (c) base metal and (d) weld of the heat-treated 304SS specimens. Vertical red lines indicate the observed paths for line profiling

during specimen preparation contributed to crack formation.

Although no apparent differences in oxide morphology were found between the base metal and weld, the chemical compositions of the oxide layer varied depending on the location. Fig. 6c and d show the elemental line profiles and maps for Fe, O, Ni, Cr, and Mn. At both locations, the O content increases moving from the oxide/base metal interface to the outer surface, indicating the formation of compounds with more Fe and O, such as Fe_3O_4 and Fe_2O_3. However, significant enrichment of Cr and Mn was found in the oxide layer just above the base metal interface (Fig. 6c). This behavior was absent in the weld (Fig. 6d). The Cr- and Mn-rich layer is $(Mn, Cr, Fe)_3O_4$ spinel, commonly observed during stainless steel oxidation [32,33]. Also, Cr depletion was observed in the substrate. The difference in Cr and Mn distributions in the oxide layer between the base metal and weld is attributed to grain size. Smaller grains in steels lead to faster diffusion of Cr and Mn due to a shorter lateral oxide growth distance, enabling quicker formation of the Cr- and Mn-rich oxide layer [32,34]. The average grain size in the weld, measured by EBSD, is 69.3 mm, which is 3.3 times larger than that in the base metal. The larger grains in the weld resulted in slower Cr diffusion, leading to an oxide layer with lower Cr content. This contributed to reduced oxidation resistance and a slightly thicker oxide layer in the weld.

Another notable point is the Ni distribution; a network-shaped Ni-rich metallic phase was observed within the oxide layer. Studies have reported that Ni-rich metallic phases act as diffusion barriers, with minimal involvement

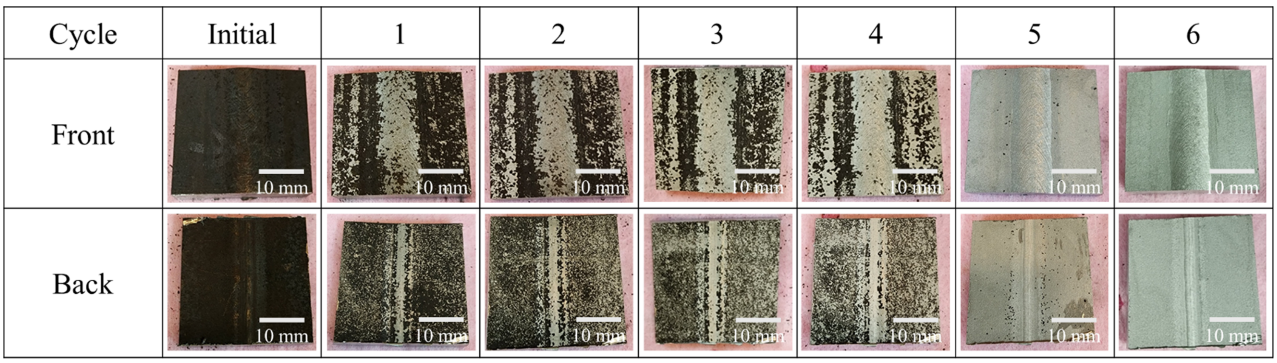

Fig. 7. Changes in the surface of the 304SS specimens after each acid pickling cycle. The numbers denote the pickling cycles

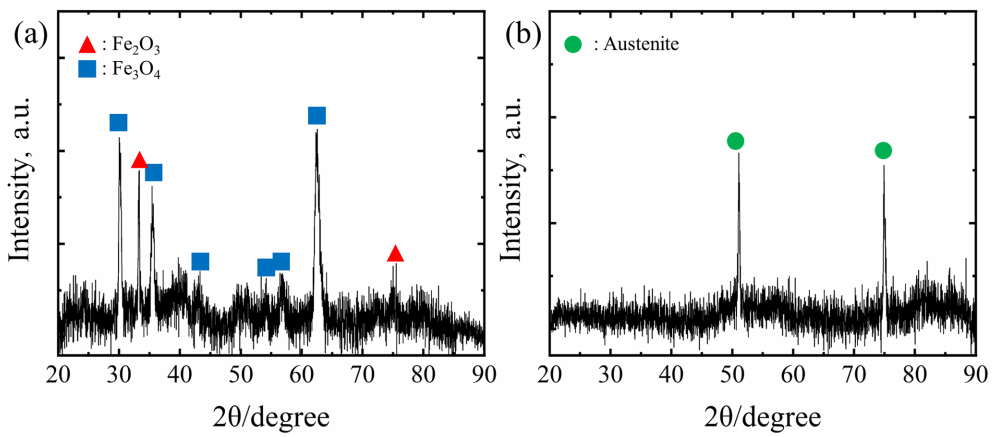

Fig. 8. X-ray diffraction patterns of the specimens (a) before and (b) after acid pickling

in oxidation [35]. The formation of $(Mn, Cr, Fe)_3O_4$ spinel during oxidation displaces Ni into the surrounding austenite, as Ni has a lower oxygen affinity than other elements. This Ni-rich metallic phase diffuses outward into the oxide layer, forming a continuous network [33,36]. Furthermore, the location of Ni-rich metallic phase depends on the oxidation temperature. Ni enrichment occurs below 500 ºC in steam, while Ni diffuses throughout the oxide layer at higher temperatures [37]. Since the specimens were heat-treated at 1050 ºC, Ni-rich regions were observed throughout the oxide layer. Additionally, nano-sized pores were observed in the upper section of the oxide layers, while the inner section was relatively dense (Fig. 6c and d) [37].

Surface changes after each acid pickling cycle, up to six cycles, are shown in Fig. 7. The initial surface was dark, with the weld and substrate indistinguishable. After the first cycle, the oxide layer on the weld began peeling off on both the front and back sides. The dissolution rate of the FeO layer depends on the acid diffusion rate through cracks and pores and the rate at which the spent acid diffuses away from the layer [16]. Acid penetrates the oxide layer through existing cracks and small pores (Fig. 6). Moreover, the oxide layer with lower Cr content near the base metal/oxide interface likely provides lower corrosion resistance in the weld (Fig. 6d). This could explain the faster peeling of the oxide layer on the weld compared to the base metal. From the second to fourth cycles, the substrate was exposed, though no apparent change was observed. After brushing the specimen surface following the fifth cycle, most of the oxide layer was removed. The remaining black dots and stains were completely eliminated after the sixth cycle.

The specimen surfaces were analyzed by XRD (Fig. 8a), showing that the main phase of the oxide layer was Fe_3O_4 with small amounts of Fe_2O_3 after heat treatment. FeO forms as a very thin layer on the steel surface at the initial stage of oxidation and is easily transformed into oxides with higher oxygen content (Fe_3O_4 and Fe_2O_3). Due to its thinness and position, FeO was not detected in

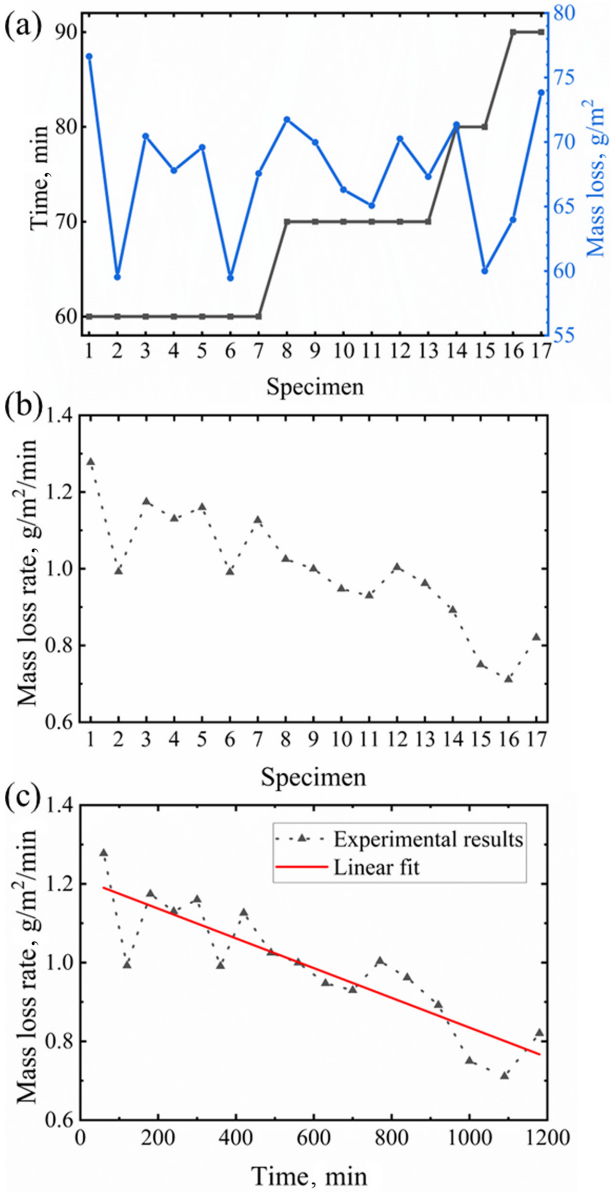

Fig. 9. (a) Acid pickling time and mass loss per specimen, and mass loss rate (b) of each specimen and (c) at different time

the XRD analysis. The oxides were completely removed after the acid pickling cycles, revealing the underlying austenite (Fig. 8b). This confirms that acid pickling was successfully performed, achieving a fine surface quality on the 304SS specimens.

To understand changes in the pickling performance of the acid solution with varying numbers of specimens, the time spent on acid pickling and the mass loss per specimen were analyzed (Fig. 9a). For up to 7 specimens, the time required for acid pickling remained constant at 60 min, increasing to 70 min when testing 8–13 specimens. For 14–15 and 16–17 specimens, immersion times of 70 and 80 min, respectively, were needed to complete pickling. By dividing the outer surface area of the specimens, the mass loss per unit area was calculated. The mass loss was only slightly influenced by the number of specimens, ranging from 59.5 to 76.6 g/m^2. The variation in mass loss per specimen may be attributed to the brushing step used to mechanically remove the oxide layer.

The mass loss rate was estimated by dividing the mass loss by the time spent pickling each specimen, as shown in Fig. 9b. The rate decreased as the number of specimens increased. This decreasing trend was caused by an increase in the Fe^{2+} ion concentration. As more specimens were immersed in the solution, a greater amount of the oxide layer dissolved, releasing iron ions. The pickling temperature of 60 ºC led to rapid and continuous evaporation of the solution, which also increased the concentration of iron ions. Using the mass loss rate and pickling time, the following linear equation was fitted:

$$r = -3.78 \times 10^{-4} t + 1.21 \quad (1)$$

where r and t are the rate in g/m^2/min and time in min, respectively. The linear fit is plotted in Fig. 9c alongside the mass loss rate over time. This equation can be used to estimate the pickling performance of the acid solution (8 vol% HF, 10 vol% H_2SO_4, and 82 vol% H_2O) and to determine when the solution should be replaced.

4. Conclusions

In this study, the effects of welding current and speed in plasma arc welding on the microstructures and mechanical properties of 304 stainless steel, as well as its acid pickling behavior, were investigated. 304 stainless steel pipes were fabricated through PAW with various welding currents and speeds. The weld consisted of austenite and δ-ferrite, with the size of the dendritic structure decreasing as heat input was reduced. The highest ductility and moderate strength were achieved with a welding current of 300 A and a welding speed of 55 cm/min. After heat treatment at 1050 ºC, an oxide layer with cracks and nanopores formed on the base metal, consisting of (Mn, Cr, Fe)$_3O_4$ spinel, Ni-rich metallic

phase, Fe_3O_4, and Fe_2O_3. The oxide layer on the weld was removed more quickly during acid pickling than that on the base metal, due to a Cr- and Mn-rich layer formed within the inner oxide. Acid pickling was successfully performed using a solution of 8 vol% HF, 10 vol% H_2SO_4, and 82 vol% H_2O. As the number of specimens increased, the time required for acid pickling also increased, while the mass loss rate decreased. An equation is proposed for estimating the pickling performance of the acid solution, which can be used to determine the appropriate time to replace the solution.

Acknowledgments

This work was supported by the Technology Innovation Program (20023954, development and demonstration of industrial IoT and intelligent system for analyzing and improving the surface quality of metal·steel products) funded by the Ministry of Trade, Industry & Energy (MOTIE, Korea).

References

1. J. R. Davis, *ASM Specialty Handbook: Stainless Steels*, 1st, ASM International (1994).
2. R. L. Plaut, C. Herrera, D. M. Escriba, P. R. Rios, A. F. Padilha, A Short Review on Wrought Austenitic Stainless Steels at High Temperatures: Processing, Microstructure, Properties and Performance, *Materials Research*, 10, 453 (2007). Doi: https://doi.org/10.1590/S1516-14392007000400021
3. S. Ghorbani, R. Ghasemi, R. Ebrahimi-Kahrizsangi, A. Hojjati-Najafabadi, Effect of Post Weld Heat Treatment (PWHT) on the Microstructure, Mechanical Properties, and Corrosion Resistance of Dissimilar Stainless Steels, *Materials Science and Engineering: A*, 688, 470 (2017). Doi: https://doi.org/10.1016/j.msea.2017.02.020
4. D. Jang, K. Kim, H. C. Kim, J. B. Jeon, D.-G. Nam, K. Y. Sohn, B. J. Kim, Evaluation of Mechanical Property for Welded Austenitic Stainless Steel 304 by Following Post Weld Heat Treatment, *Korean Journal of Metals and Materials*, 55, 664 (2017). Doi: https://doi.org/10.3365/KJMM.2017.55.9.664
5. T.-H. Nam, E. An, B. J. Kim, S. Shin, W.-S. Ko, N. Park, N. Kang, J. B. Jeon, Effect of Post Weld Heat Treatment on the Microstructure and Mechanical Properties of a Submerged-Arc-Welded 304 Stainless Steel, *Metals*, 8, 26 (2018). Doi: https://doi.org/10.3390/met8010026
6. Y. Feng, Z. Luo, Z. Liu, Y. Li, Y. Luo, Y. Huang, Keyhole Gas Tungsten Arc Welding of AISI 316L Stainless Steel, *Materials & Design*, 85, 24 (2015). Doi: https://doi.org/10.1016/j.matdes.2015.07.011
7. A. Mahrle, S. Rose, M. Schnick, E. Beyer, U. Füssel, Laser-Assisted Plasma Arc Welding of Stainless Steel, *Journal of Laser Applications*, 25, 032006 (2013). Doi: https://doi.org/10.2351/1.4798338
8. H.-Y. Huang, Research on the Activating Flux Gas Tungsten Arc Welding And Plasma Arc Welding For Stainless Steel, *Metals and Materials International*, 16, 819 (2010). Doi: https://doi.org/10.1007/s12540-010-1020-9
9. Z. M. Liu, C. S. Wu, M. A. Chen, Experimental Sensing of the Keyhole Exit Deviation from the Torch Axis in Plasma Arc Welding, *The International Journal of Advanced Manufacturing Technology*, 71, 1209 (2014). Doi: https://doi.org/10.1007/s00170-013-5568-7
10. S. Fatima, M. Khan, S. H. I. Jaffery, L. Ali, M. Mujahid, S. I. Butt, Optimization of Process Parameters for Plasma Arc Welding of Austenitic Stainless Steel (304L) with Low Carbon Steel (A-36), *Proceedings of the Institution of Mechanical Engineers, Part L: Journal of Materials: Design and Applications*, 230, 640 (2016). Doi: https://doi.org/10.1177/1464420715584392
11. D. Hipp, A. Mahrle, E. Beyer, S. Jäckel, M. Hertel, U. Füssel, Thermal Efficiency Analysis for Laser-Assisted Plasma Arc Welding of AISI 304 Stainless Steel, *Materials*, 12, 1460 (2019). Doi: https://doi.org/10.3390/ma12091460
12. P. G. Sam Infant Jones, S. Rajakumar, S. Kavitha, V. Balasubramanian, Experimental Studies on Key-Hole Plasma Arc Welding Process Parameters of AISI 304 HCu Stainless Steel Tube Joints, *Welding International*, 36, 655 (2022). Doi: https://doi.org/10.1080/09507116.2022.2151386
13. W.-S. Lee, C.-Y. Liu, C.-W. Cheng, C.-F. Lin, The Effects of Strain Rate and Welding Current Mode on the Dynamic Impact Behavior of Plasma-Arc-Welded 304L Stainless Steel Weldments, *Metallurgical and Materials Transactions A*, 35, 1501 (2004). Doi: https://doi.org/10.1007/s11661-004-0258-6
14. T. E. Abioye, I. S. Omotehinse, I. O. Oladele, T. O. Olugbade, T. I. Ogedengbe, Effects of Post-Weld Heat Treatments on the Microstructure, Mechanical and Corrosion Properties of Gas Metal Arc Welded 304 Stainless Steel, *World Journal of Engineering*, 17, 87 (2020). Doi: https:/

/doi.org/10.1108/WJE-11-2019-0323
15. S. Turgoose, W. Bullough, *11.2 - Pickling in Acid*, 11:14, L.L. Shreir, R. A. Jarman, G. T. Burstein, Butterworth-Heinemann (1994).
16. L. F. Li, J. P. Celis, Pickling of Austenitic Stainless Steels (a Review), *Canadian Metallurgical Quarterly*, 42, 365 (2003). Doi: https://doi.org/10.1179/cmq.2003.42.3.365
17. H. Dong, Z. Luo, Y. Han, Y.-M. Liu, L. Sun, W.-Y. Zhai, The Influence of Pickling Treatment Parameters on the Surface State and Pre-Passivation Behavior of Super 13Cr Martensitic Stainless Steel, *Coatings*, 12, 127 (2022). Doi: https://doi.org/10.3390/coatings12020127
18. J. Peng, M. Li, Pickling Behaviour of 2205 Duplex Stainless Steel Hot-Rolled Strips in Sulfuric Acid Electrolytes, *Advances in Materials Science and Engineering*, 2020, 4562418 (2020). Doi: https://doi.org/10.1155/2020/4562418
19. H. Li, A. Zhao, Pickling Behavior of Duplex Stainless Steel 2205 in Hydrochloric Acid Solution, *Advances in Materials Science and Engineering*, 2019, 9754528 (2019). Doi: https://doi.org/10.1155/2019/9754528
20. Q. Xie, P.-Y. Shi, C.-J. Liu, M.-F. Jiang, Effects of Different Oxidants on HCl-based Pickling Process of 430 Stainless Steel, *Journal of Iron and Steel Research International*, 23, 778 (2016). Doi: https://doi.org/10.1016/S1006-706X(16)30120-0
21. L.-F. Li, M. Daerden, P. Caenen, J.-P. Celis, Electrochemical Behavior of Hot-Rolled 304 Stainless Steel during Chemical Pickling in HCl-Based Electrolytes, *Journal of The Electrochemical Society*, 153, B145 (2006). Doi: https://doi.org/10.1149/1.2177136
22. L.-F. Li, P. Caenen, M. Daerden, D. Vaes, G. Meers, C. Dhondt, J.-P. Celis, Mechanism of Single and Multiple Step Pickling of 304 Stainless Steel in Acid Electrolytes, *Corrosion Science*, 47, 1307 (2005). Doi: https://doi.org/10.1016/j.corsci.2004.06.025
23. L.-F. Li, P. Caenen, J.-P. Celis, Chemical Pickling of 304 Stainless Steel in Fluoride- and Sulfate-Containing Acidic Electrolytes, *Journal of The Electrochemical Society*, 152, B352 (2005). Doi: https://doi.org/10.1149/1.1990127
24. Y. Sugawara, W. Inoue, I. Muto, N. Hara, A Methodology for Fabrication of Highly Pitting Corrosion-Resistant Type 304 Stainless Steel by Plasma Carburizing and Post-Pickling Treatment, *Journal of The Electrochemical Society*, 165, C441 (2018). Doi: https://doi.org/10.1149/2.0081809jes
25. C. A. Huang, C. C. Hsu, The Electrochemical Polishing Behavior of Duplex Stainless Steel(SAF 2205) in Phosphoric-Sulfuric Mixed Acids, *The International Journal of Advanced Manufacturing Technology*, 34, 904 (2007). Doi: https://doi.org/10.1007/s00170-006-0654-8
26. B. S. Covino, J. V. Scalera, T. J. Driscoll, J. P. Carter, Dissolution Behavior of 304 Stainless Steel in HNO_3/HF Mixtures, *Metallurgical Transactions A*, 17, 137 (1986). Doi: https://doi.org/10.1007/BF02644450
27. ASTM E8/E8M-22, Standard test methods for tension testing of metallic materials (2022). Doi: https://doi.org/10.1520/E0008_E0008M-22
28. S. Kumar, A. S. Shahi, Effect of Heat Input on the Microstructure and Mechanical Properties of Gas Tungsten Arc Welded AISI 304 Stainless Steel Joints, *Materials & Design*, 32, 3617 (2011). Doi: https://doi.org/10.1016/j.matdes.2011.02.017
29. S. Sabooni, F. Karimzadeh, M. H. Enayati, A. H. W. Ngan, H. Jabbari, Gas Tungsten Arc Welding and Friction Stir Welding of Ultrafine Grained AISI 304L Stainless Steel: Microstructural and Mechanical Behavior Characterization, *Materials Characterization*, 109, 138 (2015). Doi: https://doi.org/10.1016/j.matchar.2015.08.009
30. X. Li, F. Gao, J. Jiao, G. Cao, Y. Wang, Z. Liu, Influences of Cooling Rates on Delta Ferrite of Nuclear Power 316H Austenitic Stainless Steel, *Materials Characterization*, 174, 111029 (2021). Doi: https://doi.org/10.1016/j.matchar.2021.111029
31. Y. Hao, J. Li, X. Li, W. Liu, G. Cao, C. Li, Z. Liu, Influences of Cooling Rates on Solidification and Segregation Characteristics of Fe-Cr-Ni-Mo-N Super Austenitic Stainless Steel, *Journal of Materials Processing Technology*, 275, 116326 (2020). Doi: https://doi.org/10.1016/j.jmatprotec.2019.116326
32. J.-H. Kim, D.-I. Kim, S. Suwas, E. Fleury, K.-W. Yi, Grain-Size Effects on the High-Temperature Oxidation of Modified 304 Austenitic Stainless Steel, *Oxidation of Metals*, 79, 239 (2013). Doi: https://doi.org/10.1007/s11085-012-9347-x
33. A. Col, V. Parry, C. Pascal, Oxidation of a Fe–18Cr–8Ni Austenitic Stainless Steel at 850°C in O_2: Microstructure Evolution During Breakaway Oxidation, *Corrosion Science*, 114, 17 (2017). Doi: https://doi.org/10.1016/j.corsci.2016.10.029
34. R. K. S. Raman, R. K. Gupta, Oxidation Resistance of Nanocrystalline vis-à-vis Microcrystalline Fe–Cr Alloys, *Corrosion Science*, 51, 316 (2009). Doi: https://doi.org/10.1016/j.corsci.2008.10.020

35. C. Liu, P. Jin, T. Shen, Z. Wang, Microstructural Evolution of Early-Stage Oxide Film on 15–15Ti Austenitic Stainless Steel Under 500 °C Steam, *Corrosion Science*, 207, 110557 (2022). Doi: https://doi.org/10.1016/j.corsci.2022.110557
36. M. Su, J. Zhao, C. Gu, Investigation of the High-Temperature Oxidation Behavior of Fe-14Cr-9Mn-2.5Ni Austenitic Stainless Steel in N2-21 vol%O_2 Environment, *Corrosion Science*, 220, 111294 (2023). Doi: https://doi.org/10.1016/j.corsci.2023.111294
37. C. Liu, L. Qi, T. Shen, P. Jin, Z. Wang, TEM Comparative Study on Oxide Films of 316L and T91 Steel Exposed to 350–500 °C Steam, *Journal of Materials Science & Technology*, 175, 10 (2024). Doi: https://doi.org/10.1016/j.jmst.2023.07.046